4
Raman Spectroscopy: from Graphite to sp^2 Nanocarbons

This chapter gives a broad perspective on how Raman spectroscopy provides an especially sensitive characterization tool for carbon-based materials and even more so for sp^2 nanocarbon materials. Since many other optical effects can also be utilized in probing sp^2 carbons, to gain a clear understanding of the Raman scattering process, we start by contextualizing the optical processes under the broad heading of light–matter interaction phenomena. We then briefly review a number of photophysical phenomena in order to put the Raman effect into proper perspective (Sections 4.1 and 4.2). Following this discussion, we present the big picture of Raman spectra from sp^2 carbon nanomaterials (Section 4.3). The atomic vibrational nature of the modes related to each Raman peak is then introduced and the differences in the observed Raman spectra for the different sp^2 structures are addressed (Section 4.4). The presentation here is basic and follows a historic perspective, aiming to give the reader a broad picture of the Raman spectra from bulk graphite to sp^2 nanocarbons. In Chapters 5 and 6 we discuss the quantum description and selection rules for the Raman scattering process, respectively. In Part Two of the book we elaborate on the science of each Raman mode that is introduced in the present chapter, showing the great deal of information one can obtain from each of these Raman features for each specific sp^2 carbon system.

4.1
Light Absorption

When shining light into a material (molecule or solid), part of the energy simply passes through the sample (by transmission), while the remaining photons interact with the system through light absorption, reflection, photoluminescence or light scattering. The amount of light that will be transmitted, as well as the details for all the light–matter interactions will be determined by the electronic and vibrational properties of the material. Furthermore, different phenomena occur when shining light into a given material with different energy photons [1, 142], because different energies will be related to the different optical transitions occurring in the medium. As an example of the richness of light–matter interactions, a schematic optical absorption curve for a semiconducting material is shown in Figure 4.1. Using this
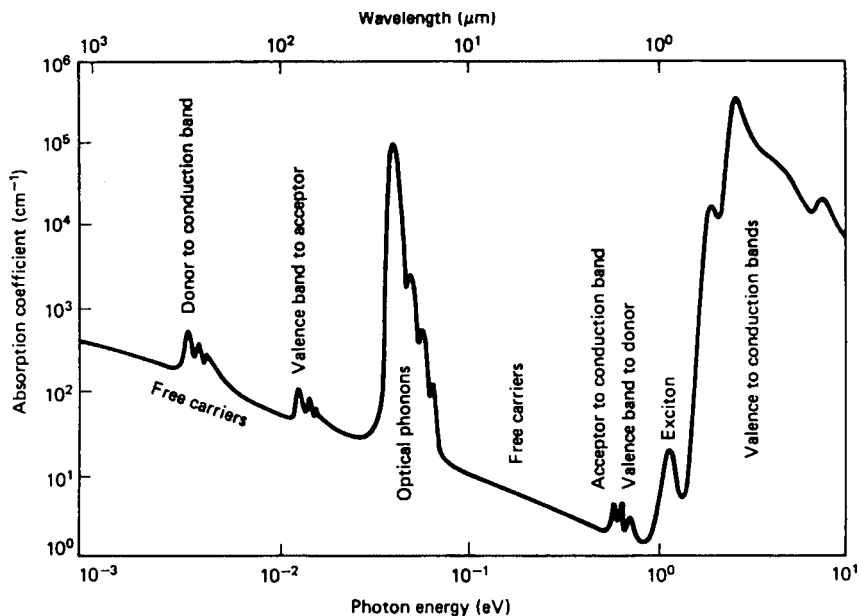
Figure 4.1 Photophysical mechanisms operative for various regions of the electromagnetic spectrum as photons in various energy ranges interact with materials.

figure as a guide, examples are given for the many different effects that might occur when light interacts with a material.

Starting from the high energy side of Figure 4.1:

- The photon (1–5 eV) can be absorbed by an electron making a transition from the valence band to the conduction band. Such a transition generates a free electron in the conduction band leaving behind a "hole" in the valence band, using the nomenclature of semiconductor physics.
- The photon with an energy smaller than the energy gap can generate an exciton level, which corresponds to an electron bound to a hole through the Coulomb interaction. Whereas excitonic levels in model semiconductor systems have excitonic levels of a few millielectron volts below the band gap, the energies in carbon nanotubes are much deeper (on the order of a few hundred millielectron volt range).
- If the semiconductor crystal contains impurities (foreign atoms), new energy levels appear in the energy band gap for an electron bound to such an impurity atom. If the impurity atom has more valence electrons than the atom it replaces, the impurity will act as an electron donor. If it has fewer electrons it will be an electron acceptor. Light can be absorbed, generating electronic transitions from the valence band to the donor impurity levels, or taking electrons from the acceptor level to the conduction band. The corresponding photon energy is 10 to 100 meV smaller than the energy gap.

- When the photon energy coincides with the energy of optical phonons (10 meV to 0.2 eV for first-order processes), light will be absorbed, thereby creating phonons. Harmonics and combination modes are observed also, extending the photon energy range to $\sim$ 350 meV. These processes occur in the infrared energy range (infrared absorption), and play a major role in the field of infrared spectroscopy.
- Shallow donor level transitions to the conduction band and valence band transitions to shallow acceptor levels can also be responsible for light absorption. The corresponding photon energy would be significantly lower than the stronger excitations from the dominant bright state. In some cases the lowest state is a dark state, which means it cannot be created by light absorption.
- The free carriers, which are electrons in metallic systems, and electrons and/or holes in doped semiconducting systems, can also absorb light, usually occurring over a broad energy range from 1 to 10 meV. Other free carrier processes not shown in the diagram also occur. In a much higher energy region (1 to 20 eV), the collective excitation of electrons also occurs. This is known as plasmon absorption.

  For the much higher energy region of ultraviolet and X-ray electron excitation (not shown in Figure 4.1), transitions from core levels also occur. In this case we observe the photoexcited electrons using experimental techniques known as ultra-violet photoelectron spectroscopy (UPS) and X-ray photoelectron spectroscopy (XPS).

One important aspect of optical absorption by crystals is related to wave vector or crystal momentum conservation. In the visible range, the wavelength of light is on the order of $\lambda_{\text{light}} \sim 500$ nm. The dimensions of the Brillouin zones are defined by the maximum value of the wave vector k, which is usually given by $k_{\text{BZ}} = \pi/a$ (see Section 2.1.5), where the primitive translation vector a in the unit cell is about 0.1 to 0.2 nm. Therefore, the photon wave vector is related to the maximum dimension of the Brillouin zone (k_{BZ}) by

$$k_{\text{light}} = \frac{2\pi}{\lambda_{\text{light}}} \approx \frac{k_{\text{BZ}}}{3000} \ . \tag{4.1}$$

Since $k_{\text{light}} \ll k_{\text{BZ}}$, we say that a photon excites one electron from the valence band to the conduction band with the same k. The transition is vertical in the electron energy dispersion, that is, there is no change of wave vector in the electronic energy dispersion.

4.2
Other Photophysical Phenomena

Section 4.1 describes schematically various mechanisms that are responsible for the optical absorption of light in a semiconducting material, as displayed in Fig-
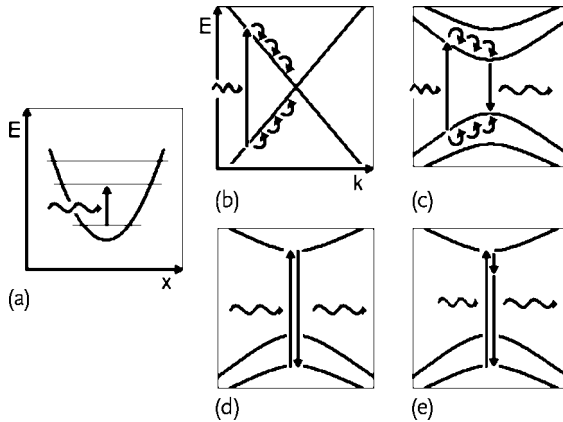
Figure 4.2 The light–matter interaction, showing the most commonly occurring processes. The waved arrows indicate incident and scattered photons. The vertical arrows denote the light-induced transitions between (a) vibrational levels (see Figure 3.2) and (b–e) electronic states. Curved arrow segments indicate electron–phonon (hole–phonon) scattering events. In (e) the shortest vertical arrow also indicates an electron–phonon transition in Raman scattering. In (d) and (e) the processes will be resonant if the incident (or scattered) light energy exactly matches the energy difference between initial and excited electronic states. When far from the resonance window where resonance occurs, the transition is called virtual. The intensity for resonance Raman scattering can be much larger for the vertical processes.

ure 4.1. Now we broadly discuss different phenomena occurring via light–matter interactions (see Figure 4.2):

- The photon energy that has been absorbed can in one case be transformed into atomic vibrations, that is, heat. When the light energy matches the energy for allowed phonon transitions, the photon can transfer energy directly to create an acoustic or optical phonon (see Figure 4.2a). This resonance process is called infrared (IR) absorption, since phonon energies occur at infrared frequencies.
- Even if the photon energy does not match the energy of the optical phonons, this photon energy can be transferred to the electrons. The photoexcited electrons then lose energy by creating multiple phonons of different frequencies by electron–phonon coupling. In a metal, such photoexcited electrons will decay down to their ground states through electron–phonon coupling in a process as shown in Figure 4.2b. If the material has an energy gap between the occupied (valence) and unoccupied (conduction) bands, the photoexcited electron can decay first to the bottom of the conduction band by an electron–phonon process and then to its ground state by emitting a photon with the band gap energy, (see Figure 4.2c). This process is called photoluminescence.
- A photon may be virtually absorbed by a material (not real absorption), which means the photon (oscillating electric field) just shakes the electrons, which will then scatter that energy back to another photon with the same energy as the incident one. In the case where the incident and scattered photons have the

same energy, the scattering process is said to be "elastic" and is named Rayleigh scattering (see Figure 4.2d).

- The photon may shake the electrons, again with no real absorption, thereby causing vibrations of the atoms at their natural vibrational frequencies (by generating phonons). In this case, when the electrons scatter the energy back into another photon, this photon will have lost (gained) energy to (from) the vibration of the atoms. This is an inelastic scattering process that creates or absorbs a phonon and it is named Raman scattering (see Figure 4.2e). When the photon loses energy in creating a phonon we call this a Stokes process. When the photon gains energy by absorbing a phonon we call the process an anti-Stokes process. Since an additional phonon energy E_{ph} is needed for the anti-Stokes process, this process is temperature-dependent and is proportional to $\exp(-\hbar\omega_{ph}/kT)$.
- In a solid, a further distinction is made between inelastic scattering by acoustic phonons (called Brillouin scattering) and by optical phonons (called Raman scattering). This concept does not apply to molecular systems where the acoustic phonon would represent a translation of the molecule (see Section 3.1.2). It is important to remember that Raman and Brillouin scattering also denote light scattering processes due to other elementary excitations in solids and molecules, but in this book we restrict the discussion of Raman scattering to the most general inelastic scattering processes that occur by optical phonons.

Many other processes not listed here, usually related to nonlinear optics, may also occur. They are usually less important for the energetic balance of the light–matter interaction and are not treated in this book. Besides, it is important to draw a distinction between Raman scattering (Figure 4.2e) and photoluminescence (Figure 4.2c), as illustrated in Figure 4.3 [143]. Several light scattering peaks are highlighted by circles in Figure 4.3b. The vertical gray band in Figure 4.3a denotes photoluminescence emission at the band gap $E_{PL} = E_{11} = 1.26\,\text{eV}$. The horizontal gray bands denote nearly continuous luminescence emission associated with thermally excited processes involving different phonon branches. The cutoff energy at 1.06 eV is marked in Figure 4.3b by a vertical dotted line. Slanted dotted lines denote emission from resonant Raman scattering processes for three different phonons named G-band, M-band, and G′-band in Figure 4.3b. Notice in Figure 4.3a the strong emission spots at E_{11} where these Raman lines cross E_{11}. These intersection points are denoted by circles in Figure 4.3b. They are associated with a mixture of photoluminescence and resonance Raman scattering processes, which differ in linewidth (Raman peaks are much sharper) and by the fact that, when changing the excitation laser line, the photoluminescence (PL) emission is fixed at E_{11}, while the Raman peaks change in absolute frequency, keeping fixed the energy shift from the excitation laser line. Occurring at the same energy, these two processes are sometimes confused in the literature, and the major reason is that Raman scattering in solids often has a much greater (say, 10^3 times larger) intensity when the photon energy is equal to an energy band gap, and this effect is called *resonant Raman scattering* (RRS) [144]. To differentiate between these processes one can just look at what happens when changing the excitation laser energy. Alterna-
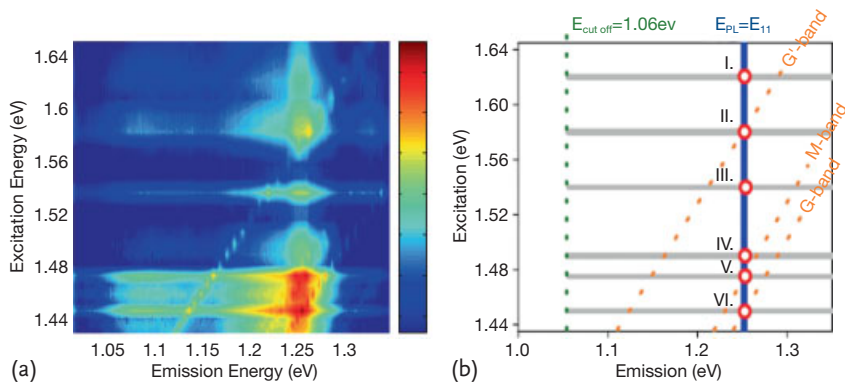
Figure 4.3 (a) A 2D excitation vs. emission contour map for a (6,5)-enriched DNA-SWNT sample. The spectral intensity is plotted using the log scale shown on the right. (b) A schematic view of the observed light emissions plotted as the excitation energy vs. photon emission energy. See the description of the different processes in the text [143].

tively, PL bands are usually broad (hundreds of cm^{-1} or larger) while Raman peaks are sharp (tens of cm^{-1} or sharper).

The difference in linewidth between Raman and PL arises because, in Raman scattering, the intermediate states that are excited between the initial state (incident photon plus the energy of the system before light absorption) and the final state (emitted photon plus the energy of the system after light emission) are "virtual" states. These virtual states do not have to correspond to real states (that is eigenstates) of the physical "system" – any optical excitation frequency will, in principle, suffice. In photoluminescence, on the other hand, the optically excited state must be a real state of the system and, in this case, a real absorption of light occurs, followed by a real emission at a different frequency. Here "real absorption" means that the photoexcited electron can be in the excited states for a sufficient time for measurement, for example, 1 ns.

4.3
Raman Scattering Effect

Within the optical processes, light scattering techniques provide an exceedingly useful tool to study fundamental excitations in solids and molecules, because light can be scattered inelastically so that the incident and scattered photons have different frequencies and this frequency difference is related to the properties of each material. The inelastic scattering of light is called the Raman effect, named in honor of the discoverer of the Raman effect in 1927, is commonly attributed to Sir Chandrasekhara Venkata Raman (1988–1970), an Indian scientist for whom the effect is named.[1]

---

1) Sir C. V. Raman was awarded the Nobel Prize of Physics in 1930 for his work on "the scattering of light" and for the discovery of the effect named after him.
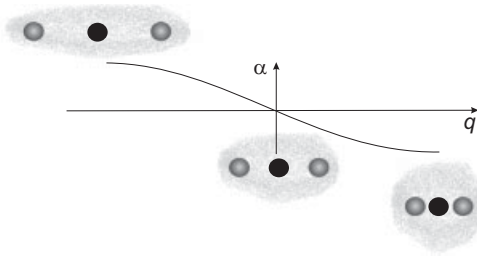
Figure 4.4 Schematics showing how the bond stretching in the CO_2 molecule changes the polarizability α of the molecule. When the oxygen atoms move farther from and closer to the carbon atom, it will be respectively eas-ier and harder for the electric field to mode the electron clouds and thus polarize the molecule. Therefore the polarizability under-goes an oscillatory behavior with the molecule vibration.

In the Raman process, an incident photon with energy $E_i = E_{laser}$ and momentum $k_i = k_{laser}$ reaches the sample and is scattered, resulting in a photon with a different energy E_s and momentum k_s. For energy and momentum conservation:

$$E_s = E_i \pm E_q \quad \text{and} \quad k_s = k_i \pm q \,, \tag{4.2}$$

where E_q and q are the energy and momentum change during the scattering event induced by this excitation of the medium. Although different excitations can result from Raman scattering, the most usual scattering phenomenon involves phonons (see Chapter 3), so that E_q and q can be considered to be the energy and the momentum of the phonon that is created or annihilated in the inelastic Raman scattering event.

In Raman scattering, the photon shakes the electrons. The inelastic scattering by phonons occurs because at different atomic positions within the vibrational mode displacements of the atom, the ability of the photon to shake the electrons will be different. This "ability" to shake the electrons is measured by the polarizability (see Figure 4.4 and Section 4.3.1 for a classical description of the Raman effect). These characteristic vibrational modes are called normal modes and are related to the chemical and structural properties of materials. Since every material has a unique set of such normal modes, Raman spectroscopy can be used to probe materials properties in detail and to provide an accurate characterization of certain Raman-active phonon modes in specific materials.

4.3.1
Light–Matter Interaction and Polarizability: Classical Description of the Raman Effect

As an optical phenomena, the basic concepts of Raman spectroscopy can be intro-duced within the framework of classical electromagnetism. Concepts like dielectric constant and susceptibility are more familiar when describing optical phenomena, but the introduction of the concept of the *polarizability* of a material is needed to discuss inelastic scattering. In this section we briefly discuss the polarizability of materials and give a classical description of the Raman effect.

In describing the polarizability α of an atom in a material, we start by defining α in terms of the polarization vector of the atom p and the local electric field E_{local} at the position of the atom:

$$p = \alpha\, E_{\text{local}} \,. \tag{4.3}$$

The polarizability α is an atomic property, and the dielectric constant ϵ of a material will depend on the manner in which the atoms are assembled to form a crystal. For a nonspherical atom, α is described by a tensor.[2] The polarization P of a crystal or of a molecule may be approximated by summing the product of the polarizability of the individual atoms in the crystal (or of the molecule) times the local electric fields

$$P = \sum_j N_j\, p_j = \sum_j N_j\, \alpha_j\, E_{\text{local}}(j) \,, \tag{4.4}$$

where N_j is the atomic concentration of each species and we sum over all the atoms in the crystal using the atomic polarization p_j given by Eq. (4.3). If the local field $E_{\text{local}}(j)$ is given by the Lorentz relation $E_{\text{local}}(j) = E + (4\pi/3)P$, then we obtain

$$P = \sum_j N_j \alpha_j \left(E + \frac{4\pi}{3} P \right) \,. \tag{4.5}$$

Solving for the susceptibility χ we then obtain

$$\chi \equiv \frac{P}{E} = \frac{\sum_j N_j \alpha_j}{1 - \frac{4\pi}{3} \sum_j N_j \alpha_j} \,. \tag{4.6}$$

Using the definition for the dielectric constant ϵ which relates the displacement vector D to the electric field E through the relation $\epsilon = 1 + 4\pi\chi$, one obtains the Clausius–Mossotti relation

$$\frac{\epsilon - 1}{\epsilon + 2} = \frac{4\pi}{3} \sum_j N_j \alpha_j \,, \tag{4.7}$$

which relates the dielectric constant ϵ to the electronic polarizability α, but only for crystal structures for which the Lorentz local field relation applies.

Light scattering can then be understood simply on the basis of classical electromagnetic theory. When an electric field $\boldsymbol{E}$ is applied to a solid, a polarization $\boldsymbol{P}$ results

$$\boldsymbol{P} = \overleftrightarrow{\alpha} \cdot \boldsymbol{E} \,, \tag{4.8}$$

2) In this case, the second-rank tensor α is a 3 × 3 matrix. When we consider p and E_{local} using another coordinate system, each component of the p and E_{local} vectors is transformed by a unitary matrix U, representing rotation, inversion, etc., such as $U p$ and $U E_{\text{local}}$. Then α is transformed by the unitary transformation $U \alpha U^{-1}$, which preserves length scales. A matrix which transforms as $U \alpha U^{-1}$ for a transformation of coordinates is defined as a second-rank tensor. p and E_{local} are both vectors and are called first-rank tensors since U appears once under a coordinate or more general unitary transformation.

where $\overset{\leftrightarrow}{\alpha}$ is the polarizability tensor of the atom in the solid, indicating that positive charge moves in one direction and negative charge moves in the opposite direction under the influence of the applied field. We now use these results to obtain a classical description for the Raman effect.

In light scattering experiments, the electric field of the light is oscillating at an optical frequency ω_i

$$\boldsymbol{E} = \boldsymbol{E}_0 \sin \omega_i t \,. \tag{4.9}$$

The lattice vibrations in the solid with a frequency ω_q modulate the polarizability of the atoms α, where

$$\alpha = \alpha_0 + \alpha_1 \sin \omega_q t \,, \tag{4.10}$$

and ω_q is a normal mode frequency of the solid that couples to the optical field so that the polarization which is induced by the applied electric field becomes:

$$\begin{aligned} \boldsymbol{P} &= \boldsymbol{E}_0(\alpha_0 + \alpha_1 \sin \omega_q t) \sin \omega_0 t \\ &= \boldsymbol{E}_0 \left[\alpha_0 \sin(\omega_i t) + \frac{1}{2}\alpha_1 \cos(\omega_i - \omega_q)t - \frac{1}{2}\alpha_1 \cos(\omega_i + \omega_q)t \right] \,. \end{aligned} \tag{4.11}$$

Thus, we see from Eq. (4.11) that light will be scattered both elastically at a frequency ω_i (Rayleigh scattering) and also inelastically, being downshifted by the natural vibration frequency ω_q of the atom (i. e., by the Stokes process for the emission of a phonon) or upshifted by the same frequency ω_q (by the anti-Stokes process for the absorption of a phonon). For a good appreciation of α_1, it is necessary to introduce quantum theory, and this is the subject of Chapter 5. In the present chapter we simply introduce the basic concept of Raman spectroscopy. In Section 4.3.2, we describe its general characteristics.

4.3.2
Characteristics of the Raman Effect

In this section we very briefly summarize a number of the important characteristics of the Raman Effect that will be broadly used throughout this book.

4.3.2.1 Stokes and Anti-Stokes Raman Processes
In the inelastic scattering process, the incident photon can decrease or increase its energy by creating (Stokes process) or destroying (anti-Stokes process) a phonon excitation in the medium. The plus (minus) signs in Eqs. (4.2) and inside parenthesis in Eq. (4.11) apply when energy has been received from (transferred to) the medium excited by the Raman signal. The probability for the two types of events depends on the excitation photon energy E_i in the scattered photon energy E_s and on the temperature.

The probability to annihilate or create a phonon depends on the phonon statistics, which is given by the Bose–Einstein distribution function. At a given temperature, the average number of phonons n with energy E_q is given by:

$$n = \frac{1}{e^{E_q/k_\mathrm{B} T} - 1} \,, \tag{4.12}$$

where k_B is the Boltzmann constant and T is the temperature. Since the vibrational energy E_q of the harmonic oscillator with n phonons is given by $E_q(n + 1/2)$, consequently the scattering event for having n phonons depends on the temperature. The probability for the Stokes (S) and anti-Stokes (aS) processes differs because in the Stokes process the system goes from n phonons to $n + 1$, while in the anti-Stokes process the opposite occurs. Using time reversal symmetry, the matrix elements for the transition $n \rightarrow n + 1$ (Stokes) and $n + 1 \rightarrow n$ (anti-Stokes) are the same, and the intensity ratio between the Stokes and anti-Stokes signals from one given phonon can be obtained by

$$\frac{I_S}{I_{aS}} \propto \frac{n + 1}{n} = e^{E_q/k_B T} \, , \tag{4.13}$$

where I_S and I_{aS} denote the measured intensity for the Stokes and anti-Stokes peaks, respectively.

Since Eq. (4.13) is obtained through time reversal symmetry, this relation should be applicable only when the Stokes and anti-Stokes processes are measured using different incident photon energies (different E_{laser}), that is, when the incident energy for the Stokes process matches the scattered energy for the anti-Stokes process (time reversal). However, usually this is not important, since the phonon energy is much smaller than the laser energy, so that incident and scattered energies are very close to each other. The previous assumption does not hold when resonance Raman scattering with sharp energy levels takes place. In this case, strong deviations from Eq. (4.13) can be obtained if I_S and I_{aS} are taken with the same E_{laser}. The resonance condition might not occur at the same E_{laser} for S and aS Raman scattering.

Finally, because the anti-Stokes signal is usually weaker than the Stokes process, it is usual that people only care about the Stokes spectra. Therefore, in this book, when not referring explicitly to the type of scattering process, it is the Stokes process that is being addressed.

4.3.2.2 The Raman Spectrum

A Raman spectrum is a plot of the scattered intensity I_s as a function of $E_{laser} - E_s$ (Raman shift, see Figure 4.5), and the energy conservation relation given by Eq. (4.2) is a very important aspect of Raman spectroscopy. The Raman spectra will show peaks at a phonon energy $\pm E_q$, where E_q is the energy of the excitation associated with the Raman effect. By convention, the energy of the Stokes process occurs at positive energy while the anti-Stokes process occurs at a negative energy. Thus, in the spectrometer (grating) which divides the scattered light into different directions, the anti-Stokes signal appears in the opposite position relative to the Stokes signal with respect to the central Rayleigh signal.

4.3.2.3 Raman Lineshape and Raman Spectral Linewidth Γ_q

The Raman spectrum exhibits a peak at $E_{laser} - E_s = E_q$ where the phonon excitation can be represented by a harmonic oscillator damped by the interaction with other excitations in the medium (similar to a mass-spring system inside a liquid).
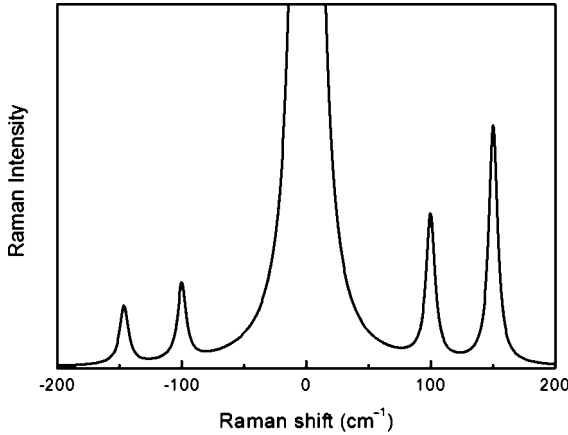
Figure 4.5 Schematics showing the Rayleigh (at $0\,\mathrm{cm}^{-1}$) and the Raman spectrum. The Rayleigh intensity is always much stronger and it has to be filtered out for any meaningful Raman experiment. The Stokes pro- cesses (positive frequency peaks) are usu- ally stronger than the anti-Stokes processes (negative frequency peaks) due to phonon creation/annihilation statistics.

Therefore, the shape of the Raman peak will be the response of a damped harmonic oscillator with eigenfrequency ω_q that is forced by an external field with a frequency ω. Considering the damping energy given by Γ_q, the power dissipated by a forced damped harmonic oscillator is a Lorentzian curve

$$I(\omega) = \frac{I_0}{\pi \Gamma_q} \frac{1}{(\omega - \omega_q)^2 + \Gamma_q^2} \, , \tag{4.14}$$

in the limit where the frequency $\omega_q \gg \Gamma_q$.[3] The full width at half maximum intensity is given by FWHM $= 2\Gamma_q$. The center of the Lorentzian gives the natural vibration frequency ω_q, and Γ_q is related to the damping or the energy uncertainty or the lifetime of the phonon [145]. Therefore, when the damping of the amplitude occurs as the scattered light energy is varied, as characterized by Γ_q, the corresponding phonon has a finite life time, Δt. The uncertainty principle $\Delta E \Delta t \sim \hbar$ gives an uncertainty in the value of the phonon energy, as measured in the Raman spectrum, which corresponds to the spectral FWHM of $2\Gamma_q$. Therefore, Γ_q is the inverse of the lifetime for a phonon, and Raman spectra in this way provide information on phonon lifetimes.

There are two main reasons for the finite phonon lifetime:

- Anharmonicity of the potential for the phonon so that, for large q far from the potential minimum, q_{eq} is no longer a good quantum number and phonon scattering occurs by emitting a phonon (third-order process) or by phonon–phonon

---

3) The solution of a forced damped harmonic oscillator is not a Lorentzian. It approaches the Lorentzian function for $\omega_q \gg \Gamma_q$. If ω_q approaches Γ_q, the lineshape departs from a Lorentzian shape.

scattering (fourth-order anharmonicity). Anharmonicity is a main contribution to the thermal expansion (third-order process) and to the thermal conductivity (fourth-order process).

• Another possible interaction is the electron–phonon interaction in which a phonon excites an electron in the valence band to the conduction band or scatters a photoexcited electron to other unoccupied states. The former electron–phonon process works for electrons in the valence band while the latter electron–phonon process associated with anharmonicity works for electrons in excited states. Thus the origin of these two electron–phonon processes are different from each other.

In specific cases, the Raman feature can deviate from the simple Lorentzian shape. One obvious case is when the feature is actually composed of more than one phonon contribution. Then the Raman peak will be a convolution of several Lorentzian peaks, depending on the weight of each phonon contribution. Another case is when the lattice vibration couples to electrons, that is, when the electron–phonon interaction takes place. In this case, additional line broadening and even distorted (asymmetric) lineshapes can result and this effect is known as the Kohn anomaly. In cases where phonons are coupled to electrons, the Raman peak may exhibit a so-called Breit–Wigner–Fano (BWF) lineshape, given by [147]:

$$I(\omega) = I_0 \frac{[1 + (\omega - \omega_{\mathrm{BWF}}/q_{\mathrm{BWF}}\Gamma_{\mathrm{BWF}})]^2}{1 + [(\omega - \omega_{\mathrm{BWF}}/\Gamma_{\mathrm{BWF}})]^2} \; , \tag{4.15}$$

where $1/q_{\mathrm{BWF}}$ is a measure of the interaction of a discrete level (the phonon) with a continuum of states (the electrons), ω_{BWF} is the BWF peak frequency at maximum intensity I_0, and Γ_{BWF} is the half width of the BWF peak. Such effects are observed in certain metallic sp^2 carbon materials and are discussed in Chapter 8, in connection with metallic carbon nanotubes.

4.3.2.4 Energy Units: cm⁻¹

The energy axis in the Raman spectra is usually displayed in units of cm^{-1}. $1\,\mathrm{cm}^{-1}$ is the energy of a photom whose wavelength is 2π cm. Lasers are usually described by the wavelength of the light, that is, in nanometers, but the phonon energies are usually too small a number when displayed in nanometers, and the Raman shifts are thus given in units of cm^{-1} ($1\,\mathrm{cm}^{-1}$ is equivalent to $10^{-7}\,\mathrm{nm}^{-1}$). Furthermore, the accuracy of a common Raman spectrometer is on the order of $1\,\mathrm{cm}^{-1}$. It is important to note that the wave number is expressed in units of cm^{-1} but the definition of the wavenumber in this case is $k = 1/\lambda$ (where λ is the wavelength of light) which is different from the definition of the wavenumber in solid state physics, $k = 2\pi/\lambda$. The energy conversion factors are: $1\,\mathrm{eV} = 8065.5\,\mathrm{cm}^{-1} = 2.418 \times 10^{14}\,\mathrm{Hz} = 11\,600\,\mathrm{K}$. Also $1\,\mathrm{eV}$ corresponds to a wavelength of $1.2398\,\mu\mathrm{m}$.

4.3.2.5   **Resonance Raman Scattering and Resonance Window Linewidth γ_r**

The laser excitation energies are usually much higher than the phonon energies. Therefore, although the exchange in energy between light and the medium is transferred to the atomic vibrations, the light–matter interaction is mediated by electrons. Usually the photon energy is not large enough to achieve a real electronic transition, and the electron that absorbs the light is said to be excited to a "virtual state", from where it couples to the lattice, generating the Raman scattering process. However, when the excitation laser energy E_{laser} matches the actual energy gap between the valence and conduction bands E_g in a semiconducting medium (or between an occupied initial state and an unoccupied final state more generally), the probability for the scattering event to occur increases by many orders of magnitude ($\sim 10^3$), and the process is then called a resonance Raman process (nonresonant otherwise). The same happens if the scattered light ($E_{\text{laser}} \pm E_q$, where "+" denotes the anti-Stokes and "−" denotes the Stokes process) is equal to the electronic transition E_g. Therefore, by varying E_{laser} through a discrete level E_g, the Raman intensity should increase when $E_{\text{laser}} \to E_g$ (resonance with incident light) and when $E_{\text{laser}} \to E_g \pm E_q$ (resonance with scattered light). A plot of the Raman intensity vs. E_{laser} gives the Raman excitation profile, according to

$$I(E_{\text{laser}}) = \left| \frac{A}{(E_{\text{laser}} - E_g - i\gamma_r)(E_{\text{laser}} - (E_g \pm E_q) - i\gamma_r)} \right|^2 . \qquad (4.16)$$

The FWHM of each peak in such a plot of the Raman excitation profile is the resonance window width γ_r, and is related to the lifetime of the excited states, that is, the lifetime for the Raman scattering process, which is the time delay between absorption of the incoming photon and emission of the outgoing photon. In other words, γ_r is the inverse of the lifetime for the photoexcited carrier. The photoexcited carrier can be relaxed from the excited states by

- The electron–phonon interaction for all possible phonons (with lifetimes < 1 ps);
- The electron–photon interaction (with lifetimes < 1 ns);
- Other excitations such as the Auger process (Coulomb interaction) (lifetime range not known yet for sp^2 carbon).

Thus the electron–phonon interaction from k (a photoexcited state) to the energy-momentum conserved $k + q$ (phonon emitting electron state) is dominant. Notice γ_r (resonance window width) is different from the Γ_q (width on the Raman intensity vs. scattered light energy Raman spectrum, where Γ_q is related to the phonon lifetime, see Section 4.3.2.3). These two experimental widths may be related or not, depending on the electron–phonon coupling. The physics behind the connection between these widths is further discussed in Part Two of this book.

The resonance effect is extremely important in nano-scale systems, since the Raman signal from nanomaterials is generally very weak because of the very small sample size. Thus the large resonance enhancement by the resonance Raman effect allows the observation of measurable Raman signals from nanostructures.

For example, the large enhancement associated with the resonance Raman scattering (RRS) process provides a means to study the Raman spectrum from a single graphene sheet, a single graphene ribbon or an individual carbon nanotube, as discussed further in Section 4.4.

4.3.2.6 Momentum Conservation and Backscattering Configuration of Light

As discussed in this section, the q vector of the phonon carries information about the wavelength of the vibration ($q = 2\pi/\lambda$) and the direction along which the oscillation occurs. In an inelastic scattering process, momentum conservation is required as given by Eq. (4.2). Different scattering geometries of light are possible by the appropriate placement of the detector of the scattered light relative to the direction of the incident light. If we select a specific choice of this geometry, we can select different phonons due to the anisotropy of the scattering event by the selection rules for Raman scattering.

In a general scattering geometry in which the scattered light wave vector $\boldsymbol{k}_s$ makes an angle ϕ with the incident $\boldsymbol{k}_i$, the modulus of the phonon wave vector q will be given by the law of cosines:

$$q^2 = k_i^2 + k_s^2 \pm 2k_i k_s \cos \phi \ . \tag{4.17}$$

The backscattering configuration of the light, for which k_i and k_s for the incident and scattered light, respectively, have the same direction and opposite signs, gives the largest possible q vector and is the most common scattering geometry when working with nanomaterials, because a microscope is usually needed to focus the incident light onto small samples and the scattered light is also collected by the same microscope.

For the Raman-allowed one-phonon scattering process, the momentum transfer is usually neglected, that is, $k_s - k_i = q \sim 0$. The momenta associated with the first-order light scattering process are on the order of $k_i = 2\pi/\lambda_{\text{light}}$, where λ_{light} is in the visible range (800–400 nm). Therefore, k_i is very small when compared to the dimensions of the first Brillouin zone, which is limited to vectors no longer than $q = 2\pi/a$, and where the unit cell vector a in real space is on the order of a tenth of a nanometer and $a = 0.246$ nm for graphene and carbon nanotubes. This discussion explains why the first-order Raman process can only access phonons at $q \to 0$, that is, very near to the Γ point. Thus, the phonon momentum $q \neq 0$ becomes important only in defect-induced or higher-order Raman scattering processes.

4.3.2.7 First and Higher-Order Raman Processes

The order of the Raman process is given by the number of scattering events that are involved in the Raman process. The most usual case is the first-order Stokes Raman scattering process, where the photon energy exchange creates one phonon in the crystal with a very small momentum ($q \approx 0$). If two, three or more scattering events occur in the Raman process, the process is called second, third, or higher-order, respectively. The first-order Raman process gives the basic quantum of vibration, while higher-order processes give very interesting information about

overtones and combination modes. In the case of overtones, the Raman signal appears at $n E_q$ ($n = 2, 3, \ldots$) and the Raman signal from combination modes appears at the sum of different phonon energies ($E_{q1} + E_{q2}$, etc.). What is an interesting point in the higher-order Raman signal in a solid material is that the restriction for $q \approx 0$ in first-order Raman scattering is relaxed. The photoexcited electron at k can be scattered to $k + q$ and can go back to its original position at k after the second scattering event by a phonon with wave vector $-q$, which allows the recombination of photoexcited electrons with their corresponding holes. The probability for selecting a pair of q and $-q$ phonons is usually small and not very important for solids. However, we will see in Chapters 12 and 13 that, under special resonance conditions (multiple resonance condition) common in sp^2 nanocarbons, we can expect a distinct Raman signal from $q \neq 0$ scattering events.

For example, in Figure 1.5, the one-phonon Raman bands in sp^2 carbons go up to frequencies of $1620\,\text{cm}^{-1}$, and the spectra above $1620\,\text{cm}^{-1}$ are composed of overtone ($G' = 2D, 2G$) and combination ($D + D'$) modes. The disorder-induced one-phonon D and D′ features are due to second-order Raman scattering process, since both features involve a scattering event by a $q \neq 0$ phonon and another scattering event induced by a symmetry breaking elastic scattering process such as a defect which contributes with a wave vector $q_{\text{defect}} = -q$, to achieve momentum conservation. The effect of defects is discussed in Chapter 13.

4.3.2.8 Coherence

It is not trivial to define whether a real system is large enough to be considered as effectively infinite and therefore to exhibit a continuous phonon (or electron) energy dispersion relation. Whether or not a dispersion relation can be defined indeed depends on the process that is under evaluation and the characteristics of this process. In the Raman process, we ask how long does it take for an electron excited by the incident photon to decay? Considering this scattering time, what is the distance probed by an electron wave function? These issues are discussed in condensed matter physics textbooks under the concept of *coherence*. The coherence time is the time the electron takes to experience an event such as a scattering process that changes its state. Thus, the coherence length is the size over which the electron maintains its quantum state identity and its coherence. The coherence length is defined by the electron speed and the coherence time, both of which can be measured experimentally. The Raman process is an extremely fast process, in the range of femtoseconds (10^{-15} s). Considering the speed of electrons in graphite and graphene (10^6 m/s), this electron speed gives a coherence length on the order of nanometers. Interestingly this number is much smaller than the wavelength of visible light. On the other hand, this is a particle picture for the scattering process and consideration of both the particle and wave aspects of electrons and phonons are important for carbon nanostructures. Playing with these concepts is actually quite interesting and important when dealing with local processes induced by defects, as is discussed in Chapter 13.

4.4
General Overview of the *sp²* Carbon Raman Spectra

Next, we provide an overview of the Raman spectra of sp^2 carbon-based materials following the basic concepts of Raman spectroscopy described above. Figure 1.5 shows the Raman spectra from different crystalline and disordered sp^2 carbon nanostructures in comparison to graphite and amorphous carbon. In the present section we will introduce the spectral features observed in the Raman spectra of many sp^2 carbons, following a historic perspective, that is, starting from the precursor material graphite, going through nanotubes and ending with the most fundamental material, graphene.

4.4.1
Graphite

The Raman spectrum of crystalline graphite is marked by the presence of two strong peaks centered at $1580 \, \text{cm}^{-1}$ and $2700 \, \text{cm}^{-1}$, being named the G and G′ bands, respectively, where the G label comes from graphite (see Figure 1.5). In 1970, Tuinstra and Koenig proposed that the lowest frequency peak (G-band, see Figure 4.6) is a first-order Raman-allowed feature originating from the in-plane stretching of the C–C bond [148, 149]. The highest frequency peak (G′ band) was reported by Nemanich and Solin [150, 151] and was then assigned as a second-order (two-phonon) feature with $q \neq 0$.

In the Raman spectra obtained from samples with small crystallite size L_a ($< 0.5 \, \mu\text{m}$, that is, smaller than the wavelength of light), the presence of an additional peak centered at $\sim 1350 \, \text{cm}^{-1}$ was observed (see Figure 4.7a). Tuinstra and Koenig assigned this feature to the breathing of the carbon hexagons that "achieves Raman activity at the borders of the crystallite areas due to loss of translational symmetry" [148, 149]. Since the frequency of this feature is about half of
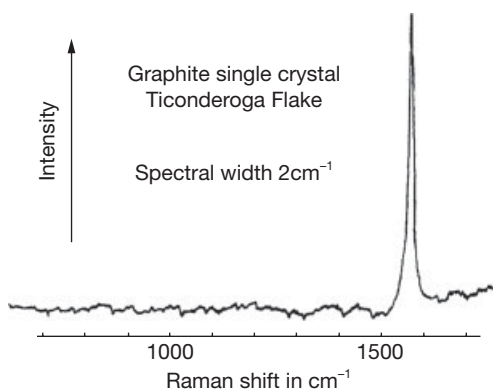

Figure 4.6 Raman spectrum from a single crystal of graphite, in which the presence of the one-phonon allowed G-band is observed [148].
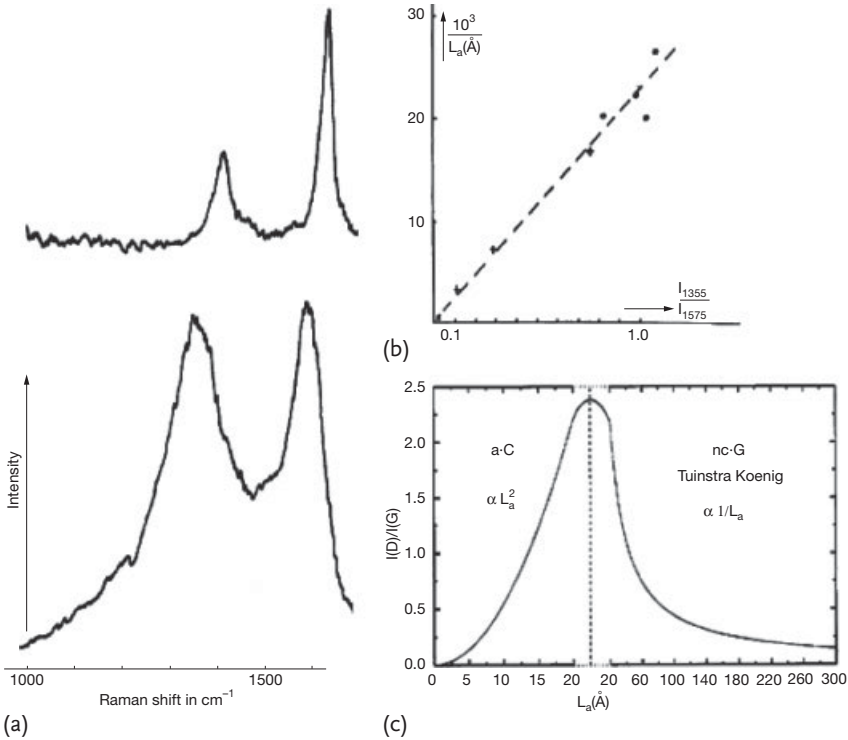
Figure 4.7 (a) Raman spectrum obtained from nanographite. The top spectrum comes from commercial graphite, and the bottom spectrum from activated charcoal. The x-axis gives the Raman shift in cm⁻¹. (b) X-ray data for L_a plotted as a function of the measured second-order G′ frequency, it was identified as the first-order of the G′ peak. Since the $1350 \, cm^{-1}$ peak is observed in the presence of defects in an otherwise perfect infinite graphite structure, it has been named the D-band (D for defect or disorder). Based on the assumption that this D-band is also associated with boundaries and interfaces, they proposed that its intensity should be proportional to the amount of crystallite boundary in the sample, and showed that the ratio between the intensities of the disorder-induced D-band and the first-order graphite G-band (I_D/I_G) is linearly proportional to the inverse of the crystallite size L_a (see Figure 4.7b) [148, 149]

intensity ratio I_D/I_G between the disorder-induced (D) and the Raman-allowed (G) peaks [148]. (c) The proposed amorphitization trajectory for I_D/I_G over a wide range of L_a (Å) values [88].

$$I_D/I_G = \frac{A}{L_a} , \tag{4.18}$$

where A is a constant for a fixed Raman excitation frequency. This relation can be applied to large enough carbon sp^2 crystallites, while the complete amorphitization trajectory for I_D/I_G going down to small L_a values was proposed in 2000 by Ferrari

and Robertson [88] (see Figure 4.7c). As proposed by Ferrari and Robertson, I_D/I_G starts to decrease for sp^2 carbon hexagonal structure starts to disappear. Furthermore, this I_D/I_G intensity ratio was further shown to be excitation laser energy-dependent [152]. Another disorder-induced band centered at 1620 cm^{-1} is usually observed in the Raman spectra of disordered graphitic materials, although with smaller intensity as compared to the D-band. This feature, reported in 1978 by Tsu *et al.* [153], has been named the D$'$-band and also depends on L_a and E_{laser} [153].

In 1981, Vidano *et al.* [154] showed that the D and G$'$-band are dispersive, that is, their frequencies change with the incident laser energy E_{laser} [154] with $\Delta\omega_D/\Delta E_{laser} \sim 50$ cm^{-1}/eV and $\Delta\omega_{G'}/\Delta E_{laser} \sim 100$ cm^{-1}/eV. The out-of-plane stacking order has also been shown to affect the G$'$ Raman spectra [155–157]. Baranov *et al.* [158] proposed, in 1987, that the dispersive behavior of the D-band comes from the coupled resonance between the excited electron and the scattered phonons, as previously discussed in semiconductor physics [91, 142]. The full appreciation of the double resonance model came in 2000, as discussed by Thomsen and Reich [159], and extended to explain the mechanism behind many other dispersive Raman peaks usually observed in the literature [160], yielding an explanation for all the features observed in the Raman spectra of ordered and disordered graphite [88]. Many of the weak Raman features are dispersive and can be used to measure the graphite phonon dispersion [160], that is, the atomic vibrations with different wave vectors, usually obtained only with inelastic neutron scattering due to momentum conservation requirements. Another interesting result obtained by the double resonance model (see Chapter 13) was the definition of the atomic structure at graphite edges [161].

In parallel to the solid state physics approach for exhibiting the Raman spectra of sp^2 carbons, a molecular approach to the Raman spectroscopy of graphite has developed based on polycyclic aromatic hydrocarbons (PAH) [162–164]. Here PAH denotes a class of planar two-dimensional π-conjugated structures consisting of condensed aromatic rings, with a structure similar to graphene (see Figure 4.8). The PAHs can be synthesized with well-defined size and shape [165, 166], allowing study of the effects of the confinement and de-localization of π-electrons using quantum chemistry calculations. The quantum chemical studies show two collective vibrational displacements characteristic of PAHs giving rise to strong Raman signals, the first appearing in the frequency range 1200–1400 cm^{-1}, with a large projection of a totally symmetric atomic vibration related to the D-band, and the second appearing in the frequency range 1600–1700 cm^{-1}, with a large projection on the G-band displacement (see Figure 4.8). The D-like band is active in PAHs due to the relaxation of the structure correlated with the confinement of π electrons. The confinement and de-localization effects can be induced in the presence of finite-size graphite domains or edges. These effects change progressively with the molecular size in connection with disordered and nanostructured sp^2 carbon materials, and exhibit a clear size-dependent resonance phenomenon. These concepts have been behind the development of long-range electron–phonon coupling models for the periodic graphene structure, such as for the Kohn anomaly, discussed in Chapter 8 [141].
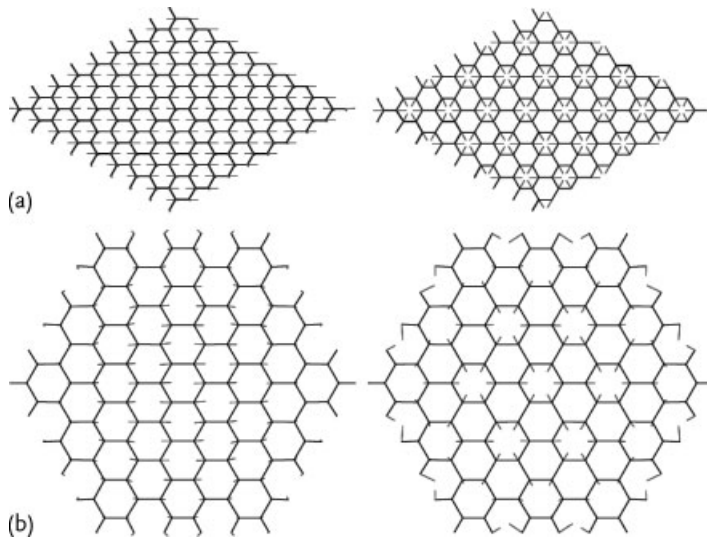
Figure 4.8 (a) nuclear displacements associated with the G-band (at Γ point) and D-band phonons (at the *K* point) of a perfect 2D graphene monolayer. (b) comparison with selected normal modes of $C_{114}H_{30}$, as obtained from semi-empirical quantum consistent-force-field π electron method (QC FF/PI) calculations [167].

At this point, the main ingredients responsible for the large impact of Raman spectroscopy on sp^2 nanocarbons are already in place. The G-band gives the first-order signature. As we will see, the G-band exhibits a rich behavior for nanostructured systems due to quantum confinement effects, curvature effects and electron–phonon coupling. The G′-band is sensitive to small changes in both the electronic and vibrational structures, and acts as a probe for electrons and phonons and their uniqueness in each distinct sp^2 nanocarbon. The disorder-induced D-band (and also the smaller intensity D′-band) appears due to symmetry-breaking effects, and, together with theory, can provide valuable information about local disorder. The D-band is a second-order process that includes an inelastic scattering event and thus D-band is not the first-order process of the G′-band which only involves two phonon scattering processes of the same phonon as for the D-band. Finally, many other small features can be observed and related to specific physical properties.

To conclude this brief review of the Raman spectra of graphite, we note that when strong amorphization takes place, substantially increasing the sp^3 carbon sample content, significant changes in the Raman lineshapes are observed [88]. Amorphous carbon and diamond-like materials have been intensively studied and these materials have been broadly utilized in surface coating applications. This book will discuss in depth the disorder-induced features related to symmetry breaking of the sp^2 configuration, but discussion of the Raman spectra associated with amorphization is beyond the scope of this volume. For more discussion on sp^3 carbon systems, see for example [88].

4.4.2
Carbon Nanotubes – Historical Background

The use of Raman spectroscopy to characterize carbon materials generally [90, 168] motivated researchers to apply this technique also to SWNTs shortly after the early synthesis of SWNTs in 1993 [25, 26]. Even though only $\sim 1\%$ of the carbonaceous material in the sample used in the 1994 experiments was estimated to be due to SWNTs [169], a unique Raman spectrum was observed, different from any other previously observed spectrum, namely a double-peak G-band structure. These findings motivated further development of this noninvasive characterization technique for SWNTs, and the laser ablation technique, developed in 1996 to synthesize large enough quantities of high purity SWNT material [170], opened up this field of investigation [136].

The first phase explorations of Raman spectroscopy on SWNTs spanned the four year period 1997–2001. Figure 4.9 gives a general view of the Raman spectra from a typical SWNT bundle sample. There are two dominant Raman signatures in these Raman spectra that distinguish a SWNT from other forms of carbon. The first relates to the low frequency feature, usually in the range 100–300 cm^{-1}, arising from phonon scattering by the radial breathing mode (RBM), which corresponds to symmetric in-phase displacements of all the carbon atoms in the radial direction
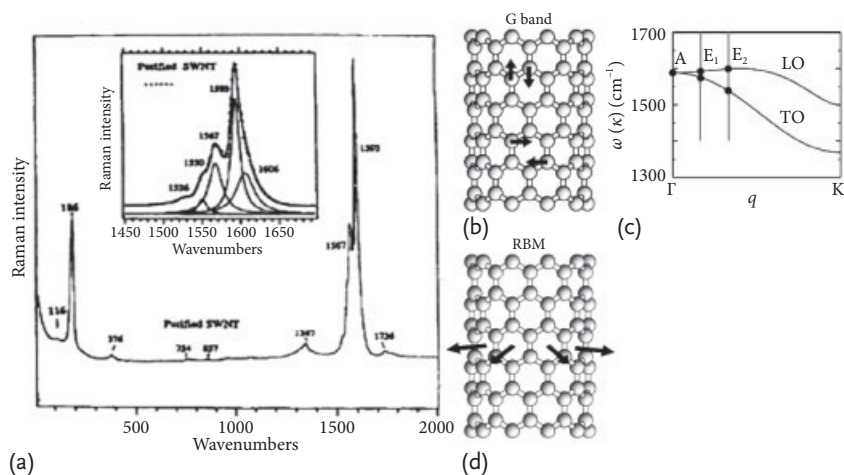

Figure 4.9 (a) Room temperature Raman spectrum from a SWNT bundle grown by the laser vaporization method. The inset shows a Lorentzian fit to the G-band multiple feature [112, 136]. (b) The G-band eigenvectors for the C–C bond stretching mode. The G-band is composed of up to six peaks that are allowed in the first-order Raman spectra. The vibrations are tangential to the tube surface, three along the tube axis (LO) and three along the circumference (TO), having two modes with A, E_1 and E_2 symmetries. Within the set of three peaks, what changes is the relative phase of the vibration, containing 0, 2 or 4 nodes along the tube circumference, which is related to increasing q in the unfolded graphene phonon dispersion $\omega(q)$ along ΓK in the Brillouin zone (c). (d) Eigenvector for the radial breathing mode (RBM) appearing around 186 cm^{-1} in (a).

(see Figure 4.9d). The second signature relates to the multi-component higher frequency features (around 1500–1600 cm^{-1}) associated with the tangential (G-band) vibrational modes of SWNTs and is related to both the early observations in [169] and to the Raman-allowed feature appearing in Raman spectra for graphite (see Figure 4.9b,c). Neither the RBM feature nor the multi-component G-band features in the Raman spectra for SWNTs were previously observed in any other sp^2 bonded carbon material.

Like in graphite, several studies were carried out on the D, G, G′ bands of carbon nanotubes, as well as on other combination modes and overtones [112]. The power of Raman spectroscopy for studying carbon nanotubes was in particular revealed through exploitation of the resonance Raman effect, which is greatly enhanced by the singular density of electronic states, which comes from one-dimensional confinement of the electronic states. Soon after the discovery of the resonance Raman effect in SWNTs [136], it was found that the resonance lineshape could be used to distinguish metallic from semiconducting SWNTs. Specifically, the lineshape for the lower frequency G-band feature (G$^-$) is broader for a metallic tube, and this feature follows a Breit–Wigner–Fano lineshape, and downshifted in frequency from that for a semiconducting tube of similar diameter (see Figure 4.10a) [147, 171]. The RBMs from SWNT bundles were found to exhibit an oscillatory behavior depending on the excitation laser energy, due to the confinement of the electronic structure [172], and a similar effect was observed for the G′ band [173]. The interpretation of all these resonance Raman effects was systematized by the develop-
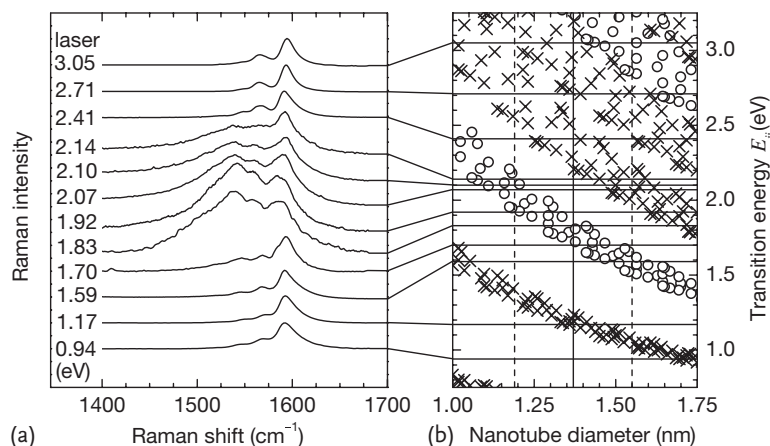

Figure 4.10 (a) Raman spectra of the tangential G-band modes of carbon nanotube bundles measured with several different laser lines showing lineshapes typical of semiconducting and metallic carbon nanotubes, taken from [171]. (b) Optical transition energies for the nanotube diameter distribution in the bundles (the vertical solid line is the average nanotube diameter and the vertical dashed lines define the full width at half maximum diameter distribution of the nanotube sample). Crosses denote optical transition energies for semiconducting nanotubes and open circles are for metallic SWNTs. The G-band gets broad and downshifted when the laser is in resonance with optical transitions from metallic SWNTs, as shown in (a) [110].

ment, in 1999, of the so-called Kataura plot, where Kataura and coworkers displayed the optical transition energies for each (n, m) SWNT as a function of tube diameter [174], as shown in Figure 4.10b. Advances in the synthesis of carbon nanotubes also took place in the 1997–2001 time frame, allowing the use of catalyzed chemical vapor deposition (CVD) techniques in the growth of samples of isolated individual SWNTs on an insulating substrate, such as oxidized silicon (Si/SiO₂) [175].

The second phase explorations of the Raman spectroscopy of SWNTs spanned the four year period 2001–2004 and this phase was opened by the observation of Raman spectra from a single isolated SWNT [176], as shown in Figure 4.11. Measurements of the frequency of the radial breathing mode and the resonant energy E_{ii} at the single nanotube level allow a determination to be made of the (n, m) in-
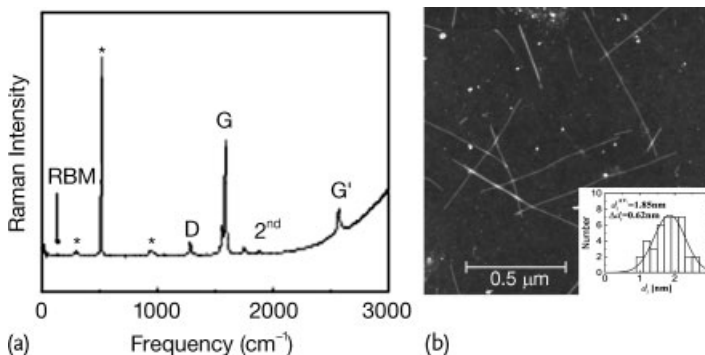

Figure 4.11 (a) Raman spectra from SWNTs at the single nanotube level. The Raman features denoted by "*" come from the Si/SiO₂ substrate on which the nanotube is mount-

ed. (b) Atomic force microscopy image of the SWNT sample used in the experiment. The inset (lower right) shows the diameter distribution of the sample in (b) [176].
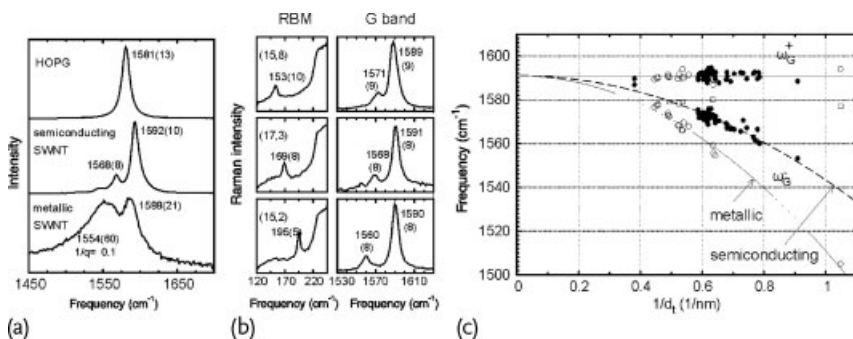

Figure 4.12 (a) The G-band for highly oriented pyrolytic graphite (HOPG), one semiconducting SWNT and one metallic SWNT. For C₆₀ fullerenes a peak in the Raman spectra is observed at 1469 cm⁻¹, but it is not considered a G-band. (b) The radial breathing mode (RBM) and the G-band Raman spectra for three semiconducting isolated SWNTs with the indicated (n, m) values. (c) Frequency vs. $1/d_t$ for the two most intense G-band features (ω_{G^-} and ω_{G^+}) from isolated semiconducting and metallic SWNTs [179].

tegers of a SWNT as a function of nanotube diameter d_t and chiral angle θ [31]. Once the (n, m) of a given tube is identified, then the dependence of the frequency, width and intensity of each of the features in the Raman spectra on diameter and chiral angle can be found, including the RBM, G-band, D-band, G′-band, and various overtone and combination modes within the first-order and higher-order frequency regimes (see Figure 4.12 for the ω_G dependence on $1/d_t$) [80, 179]. Such studies have played a major role in advancing both the fundamental understanding of Raman spectroscopy for 1D systems and in characterizing actual SWNT samples [80, 177, 178].

Third phase explorations of Raman spectroscopy on SWNTs started in 2004. It was initiated by both the development of the high pressure CO (HiPCO) and compact synthesis processes for nanotubes, that generated a large amount of SWNTs in the low diameter limit of 0.7–1.3 nm, and the development of a method for dispersing the nanotube bundles to produce isolated tubes in solution. The presence of isolated tubes with relatively small diameters allowed detailed studies to be made of the first electronic transition E_{11}^S for semiconducting nanotubes using mostly photoluminescence experiments [180] ($E_{ii} \propto 1/d_t$, E_{11}^S being in the far-infrared spectral range for usual tube diameters $d_t > 1.3$ nm). Studies on the small diameter SWNTs led to an observation of the departure from the tight-binding model which predicted the "ratio rule", that is, $E_{22}^S/E_{11}^S = 2$ for armchair tubes [181]. The observation of $2n + m$ family effects [180, 182] led to much more sophisticated first principles and tight-binding models for treating many-body effects in 1D systems.

In order to accurately study the optical transition energies, resonance Raman experiments with many laser lines and tunable laser systems (based on dye lasers and Ti:Sapphire laser systems) started to be made [183, 184]. Using several closely spaced excitation laser energies, 2D plots were made from the RBM spectra obtained from Stokes resonance Raman measurements as a function of E_{laser}. Figure 4.13a presents a map of Stokes resonance Raman measurements of carbon nanotubes grown by the HiPCO process, dispersed in aqueous solution and wrapped with sodium dodecyl sulfate (SDS) [185], in the frequency region of the RBM features, built from 76 values of E_{laser} for $1.52 \leq E_{\text{laser}} \leq 2.71$ eV. Several RBM peaks appear in Figure 4.13a, each peak corresponding to an (n, m) SWNT in resonance with E_{laser}, thereby delineating for each nanotube both the resonance spectra as a function of E_{laser} and the resonance window (Raman intensity as a function of the energy in the range where the RBM feature can be observed).

Figure 4.13b shows a comparison between the experimental and theoretical Kataura plots. The filled circles are experimental E_{ii} vs. ω_{RBM} obtained by Telg *et al.* [184] from analysis of an experiment very similar to the one performed by Fantini *et al.* [183] and shown in Figure 4.13a. The open circles come from a third-neighbor tight-binding calculation [184]. Black and gray open circles represent, respectively, M-SWNTs and S-SWNTs. The geometrical patterns for carbon nanotube families with $(2n + m) = $ constant (dashed gray lines) for E_{22}^S, E_{11}^M and E_{33}^S are also shown along with the (n, m) values assigned for some SWNTs. The energies do not match very well due to the simplicity of the TB method, even going up to third-neighbor interactions. However, the observed geometrical patterns can be
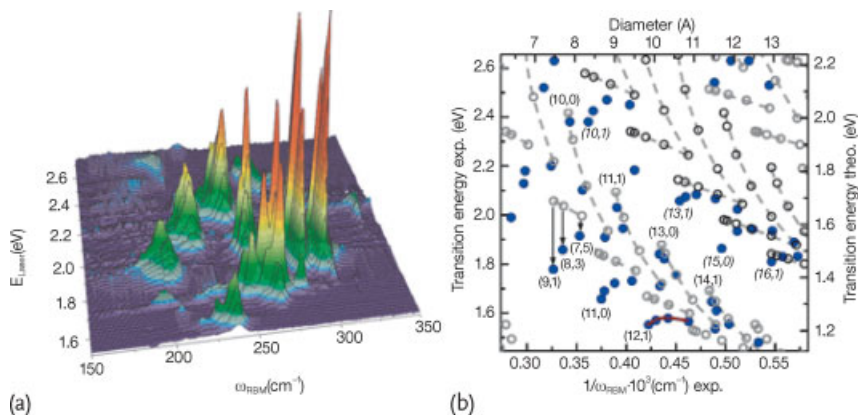
Figure 4.13 (a) RBM Raman measurements of HiPCO SWNTs dispersed in an SDS aqueous solution [185], measured with 76 different laser lines E_{laser} [183]. The nonresonance Raman spectrum from a separated CCl₄ solution is acquired after each RBM measurement, and used to calibrate the spectral intensities and to check the frequency calibration. (b) Filled circles are experimental E_{ii} vs. ω_{RBM} data obtained by Telg *et al.* [184] from analysis of an experiment very similar to the one shown in (a). The label "Transition energy exp." actually indicates the excitation laser energy (E_{laser}). Open circles come from third-neighbor tight-binding calculations, showing that even the addition of interactions with more neighbors in the π-band based tight-binding model is not enough to accurately describe the experimental results. Gray and black circles indicate calculated optical transitions from semiconducting (E_{22}^{S} and E_{33}^{S}) and metallic (E_{11}^{M}) tubes, respectively.

compared with the predicted patterns, and the comparison leads to the (n, m) assignment of individual SWNTs. Based on these results, an extended tight-binding picture, which includes σ–π hybridization due to tube curvature, strong excitonic effects of the excited electron–hole pair and the Coulomb repulsion of electrons was developed [186]. These theoretical advances allowed very accurate calculations of (n, m)-dependent resonance Raman cross-sections [187, 188]. Present work in this field has been devoted to studying effects of both the nanotube environment [189, 190] and nanotube defects [191].

4.4.3
Graphene

Among the sp^2 carbon systems, monolayer graphene is the simplest and has, consequently, the simplest Raman spectra (see Figure 4.14). Intensive graphene science study started quite recently (in 2004 [51]), but the carbon-Raman community was ready for almost instantaneous appreciation of the important achievements made in characterizing sp^2 carbons with the Raman technique [5, 86]. One interesting aspect of the graphene studies was the sudden realization of a perfect prototype system for studying sp^2 carbons. The dispersion of the G′-band by changing the excitation laser energy in bilayer graphene was used to study the effects of interlayer coupling on the *electronic* structure [192]. The effect of different substrates
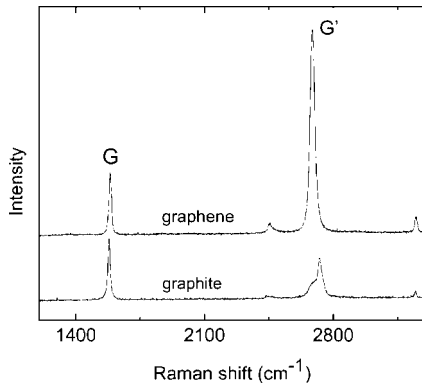
Figure 4.14 Raman spectrum of single-layer graphene in comparison to graphite measured with a 514 nm ($E_{\text{laser}} = 2.41\,\text{eV}$) laser. The two most intense features are the first-order Raman-allowed G-band and the second-order G′-band. The spectrum of pristine single-layer graphene is unique in sp^2 carbons for exhibiting a very intense G′-band as compared to its G-band feature.

and deposited top gates on the G and G′-band of graphene due to strain, charge transfer effects and disorder have been studied with unprecedented detail [193–195]. As a result of all these characterization studies, Raman spectroscopy is now being used commonly as a tool for measuring doping in graphene electronic devices [196] as well as in carbon nanotubes [191]. This is one of the many examples of how findings in graphene helped with understanding experimental results on nanotubes, and vice-versa. Because of the peculiar and unique electronic dispersion of graphene, being a zero gap semiconductor with a linear $E(k)$ dispersion relation near the Fermi level, the G-band phonons (energy of 0.2 eV) can promote electrons from the valence to the conduction band. The electron–phonon coupling in this system is quite strong, and gives rise to a renormalization of the electronic and phonon energies, including a sensitive dependence of the electronic structure on electron or hole doping [196].

Furthermore, interesting confinement and polarization effects can be observed in the G-band of a graphene nanoribbon, as shown in Figure 4.15 [83]. The lower frequency G_1-band coming from the nanoribbon on top of an HOPG substrate can be separated from the substrate higher frequency G_2-band by use of laser heating of the nanoribbon (see Figure 4.15). The temperature rise of the ribbon due to laser heating is greater than that of the substrate and therefore ω_{G_1} for the ribbon decreases more than for the substrate because of the higher thermal conductivity of the substrate relative to the graphene ribbon. The ribbon G_1-band shows a clear antenna effect, where the Raman signal disappears when crossing the light polarization direction with respect to the ribbon axis, in accordance with theoretical predictions [80].

The high sensitivity of the G′-band feature to the electronic structure was used to differentiate between 1-LG, 2-LG and many-layer graphene (see Figure 4.14) [86, 197], as well as folded (but not stacked in accordance with AB Bernal stacked
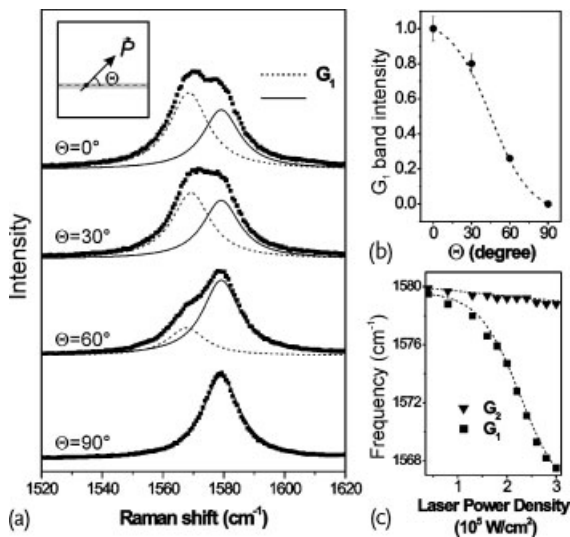
Figure 4.15 (a) The G-band Raman spectra from a graphene nanoribbon (G₁) and from the graphite substrate on which the nanoribbon sits (G₂). (b) The G₁ peak intensity dependence on the light polarization direction with respect to the ribbon axis, including experimental points on the dark curve and theoretical predictions by the dashed curve. (c) Frequency of the G-band peaks as a function of incident laser power for the graphene ribbon (G₂) in contrast to the results for the HOPG substrate (G₁) [83].

graphite) layers [198]. The Raman technique soon became the fingerprint for quick characterization of few-layer graphene samples. Raman imaging also differentiates between the number of layers in different locations of a large graphene flake, due to the dependence of the Raman intensity on the number of scattering layers [197], although this information has not yet provided an accurate characterization tool for determining the number of layers in few-layer graphene. The epitaxial growth of graphene on a SiC substrate, among others, and the effect of other chemically induced environmental interactions has also been studied using Raman spectroscopy [199].

Problems

[4-1]   This problem tests your understanding of the difference between resonance Raman scattering (RRS) and hot luminescence (PL) processes. Consider a material with a discrete optical level with energy E_g and a phonon with energy E_q. Build a plot of E_i vs. E_s and show how the PL and the RRS should appear in such a plot. Make schematic pictures to show you can differentiate the two processes when they overlap in energy.

[4-2] Obtain Eq. (4.7) from Eq. (4.6).

[4-3] Consider the equation for a damped harmonic oscillator driven by a force F_0

$$m\frac{\partial^2 x}{\partial t^2} + \gamma \frac{\partial x}{\partial t} + Kx = F_0 \exp i(\omega t + \phi) \, . \tag{4.19}$$

   a. Obtain and plot the oscillator response x as a function of the driving frequency ω.
   b. Show that the power response ($|x|^2$) exhibits a Lorentzian lineshape when the natural oscillator frequency is much larger than the peak full width at half maximum intensity. Obtain an expression for the time dependence of the full width at half maximum intensity.

[4-4] Show that 1 eV corresponds to 8065 cm^{-1}. What is the energy in eV for the G-band Raman spectrum of graphite at 1580 cm^{-1}?

[4-5] Obtain the energy in eV of a laser with a wavelength of 633 nm. What is the conversion formula from nm to eV, and from eV to nm?

[4-6] What is the wavelength of the Stokes and anti-Stokes scattered light for the graphene (1590 cm^{-1}) G-band for 514.5 nm laser light?

[4-7] When we consider the room temperature Raman spectrum for a carbon nanotube at 300 K, what is the intensity ratio of the anti-Stokes and Stokes intensities I_{aS}/I_S for the G-band (1590 cm^{-1}) and for the radial breathing mode for a 1nm diameter SWNT, with $\omega_{RBM} = 227$ cm^{-1}? When the temperature is changed to 4 K and to 2000 K, what are the new values of I_{aS}/I_S for these cases?

[4-8] Derive the relation between the Raman peak FWHM and phonon lifetime.

[4-9] Calculate the wave vectors for 488 nm, 514 nm, 633 nm lasers and compare them with the wave vector of the K and M points of graphene.

[4-10] Consider the linear dispersion of energy for graphene,

$$E(k) = \pm \frac{\sqrt{3}\gamma_0}{2} \left(\sqrt{k_x^2 + k_y^2} \right) a \, ,$$

where $\pm$ denote the valence and conduction bands, respectively, and $\gamma_0 = 2.9$ eV (nearest neighbor transfer energy for an optical transition) and $a = 0.246$ nm. Show that this energy dispersion has the shape of two cone structures with the apexes of their Dirac cones that touch each other at the K (Dirac) point. Calculate the $|k|$ value (distance from the Γ point in k space) for an optical transition observed with a 514 nm laser.

[4-11] In Problem 4-10, when an optical phonon (LO branch) with energy 1580 cm^{-1} is emitted, show the energy-momentum conserved final states

in the energy dispersion and show the possible q vectors in a figure. (Hint: the final states should be on an equi-energy contour of $E_{laser} - E_q$).

[4-12] In the case of graphene, the Dirac cone shape appears not only at the K point but also at the K' point. Explain in what ways K and K' are not equivalent to each other. If we consider the inelastic scattering from k in the K Dirac cone to $k - q$ in the K' Dirac cone, plot the possible q vectors measured from the Γ point in the two-dimensional Brillouin zone.

[4-13] In the previous problem, for a given laser excitation, the k wave vector for photoexcited electrons exists on an equi-energy contour. Plot the possible q vectors in the two-dimensional Brillouin zone.

[4-14] The condition for the resonance Raman effect is given by $E_{laser} = E_{gap}$, where E_{gap} denotes the energy separation between the conduction and valence energy bands. If the resonance condition is applied for the scattered resonance for phonon energy E_q, show the resonance condition for the scattered light, which we call the scattered light resonance condition. Explain why the scattered light resonance condition depends on the phonon energy while the incident light resonance condition does not.

[4-15] When we plot the Raman intensity as a function of E_{laser} (Raman excitation profile), we expect two peaks: one for the incident resonance and one for the scattered resonance conditions. When we have two different phonons with different phonon energies, illustrate the expected Raman excitation profiles.

[4-16] Explain the resonance conditions for anti-Stokes shifts. Illustrate two Raman excitation profiles for the Stokes and anti-Stokes Raman signals. Explain why the two Raman excitation profiles do not appear at the same excitation energy values.

[4-17] If we consider second-order Raman scattering for a $q \neq 0$ phonon for graphene, we have two distinct q vectors for a $q \neq 0$ scattering event. Explain this situation by using the two Dirac cone model. We denote these two scattering events by intravalley scattering and intervalley scattering.

[4-18] Explain the results in Problem 4-17 with an illustration of intervalley scattering for the forward (q) and backward ($-q$) scattering geometries.

[4-19] Explain in the phonon dispersion of graphene (Figure 3.1), which phonons are selected for intravalley and intervalley $q \neq 0$ scattering. Explain what happens for the case of forward and backward scattering.

[4-20] For an intravalley process, when we consider two laser energies $E_1 < E_2$, show that the q vectors are larger for $E_{laser} = E_2$. When the laser energy increases, how is the scattered q vector selected in the phonon energy dispersion?

[4-21] If E_{laser} is selected in the Raman measurement of single-wall carbon nanotubes (SWNTs), we can get a Raman signal only from SWNTs, which satis-

fy the resonance condition $E_{\text{laser}} = E_{ii}$. When we observe the radial breathing mode (RBM) whose frequency is inversely proportional to the diameter, how can we determine (n, m) values from the known calculated values of E_{ii} and ω_{RBM}? Explain a procedure that could be used to get (n, m) values.

[4-22] In order to obtain all the (n, m) values for SWNTs in a given sample, we need an almost continuously tunable energy output from E_{laser}. Suppose that you have a laser system with continuously tunable energy, how should you arrange the experimental schedule to obtain all these (n, m) values? Explain your purpose and the method you will use.

[4-23] Suppose that we have only one SWNT on a Si substrate. The position of the SWNT cannot be seen by optical microscopy. Explain why obtaining (n, m) for the specified SWNT by Raman spectroscopy is difficult. In order to overcome this difficulty, how should we prepare our samples or arrange our experimental set up?

[4-24] Try to correlate the modifications in the G$'$ feature, as shown in Figure 4.14b with the changes in the electronic structure, as discussed in Section 2.2.4.

[4-25] How should the $I_{\text{D}}/I_{\text{G}}$ intensity ratio depend on the defect density in a graphene layer? Discuss a physical picture for some defect density condition with use of some typical lengths of the system.